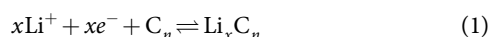


Reversible superdense ordering of lithium between two graphene sheets

Matthias Kühne^{1,6,8}, Felix Börrnert^{2,8}, Sven Fecher¹, Mahdi Ghorbani-Asl³, Johannes Biskupek², Dominik Samuelis^{1,7}, Arkady V. Krasheninnikov^{3,4,5}, Ute Kaiser^{2*} & Jürgen H. Smet^{1*}

Many carbon allotropes can act as host materials for reversible lithium uptake^{1,2}, thereby laying the foundations for existing and future electrochemical energy storage. However, insight into how lithium is arranged within these hosts is difficult to obtain from a working system. For example, the use of *in situ* transmission electron microscopy^{3–5} to probe light elements (especially lithium)^{6,7} is severely hampered by their low scattering cross-section for impinging electrons and their susceptibility to knock-on damage⁸. Here we study the reversible intercalation of lithium into bilayer graphene by *in situ* low-voltage transmission electron microscopy, using both spherical and chromatic aberration correction⁹ to enhance contrast and resolution to the required levels. The microscopy is supported by electron energy-loss spectroscopy and density functional theory calculations. On their remote insertion from an electrochemical cell covering one end of the long but narrow bilayer, we observe lithium atoms to assume multi-layered close-packed order between the two carbon sheets. The lithium storage capacity associated with this superdense phase far exceeds that expected from formation of LiC_6 , which is the densest configuration known under normal conditions for lithium intercalation within bulk graphitic carbon¹⁰. Our findings thus point to the possible existence of distinct storage arrangements of ions in two-dimensional layered materials as compared to their bulk parent compounds.

Figure 1a shows a schematic of our devices, all of which are supported by Si_3N_4 -covered Si substrates; the Si_3N_4 forms a $40\ \mu\text{m} \times 40\ \mu\text{m}$ membrane at the centre of the Si chip. A bilayer graphene flake is exfoliated from natural graphite and etched into a Hall bar shape. One end of the flake is connected to a counter electrode on the Si_3N_4 surface via a Li-ion conducting solid polymer electrolyte that has been encapsulated in a thin layer of SiO_x to avoid outgassing and oxidation in air. This setup with an electrochemical cell at the end of the flake allows for the controlled reduction/oxidation of bilayer graphene according to¹:



Using a procedure similar to that in refs ^{11,12}, we trigger lithiation (delithiation) by applying a positive voltage $U_G = 5\ \text{V}$ ($U_G = 0\ \text{V}$) to the counter electrode with respect to the bilayer graphene. A grounded current lead to the latter serves as a source/sink for the electrons required to facilitate the reversible intercalation of Li ions at the electrolyte-covered end of the bilayer graphene bar. Intercalated Li exhibits rapid lateral diffusion that tends to establish and maintain an even distribution of Li throughout the bilayer¹³. Hence, one may study its ordering in a region well separated from the electrolyte by *in situ* TEM (Fig. 1a, b), thereby also preventing exposure of the electrolyte to the electron beam. In the region probed by TEM, bilayer graphene is suspended over a hole in the Si_3N_4 membrane. Metallic contacts to the bilayer allow monitoring of its resistivity $\rho_{xx} = U_{xx}/I$ (where U_{xx} is the

longitudinal voltage drop and I is the applied current) in the electrolyte-uncovered region (Fig. 1a). During subsequent lithiation/delithiation cycles, we typically observe reversible changes in ρ_{xx} (Fig. 1c). These relate to changes in the local Li concentration via finite electronic charge transfer^{12,13}. The decrease of ρ_{xx} during lithiation reflects an increase in electron density, characteristic of ambipolar diffusion of electron–ion pairs into the probed area¹³. During delithiation, Li ions and electrons leave the bilayer, thereby restoring its initial resistivity value. The exact time evolution of ρ_{xx} depends on the kinetics of several (uncontrolled) processes, related to, for example, ionic transport within the electrolyte and across the solid electrolyte interphase. Yet the behaviour shown in Fig. 1c is a qualitative characteristic of reversible Li intercalation in bilayer graphene¹³. In the following, we present *in situ* TEM data obtained in the unique spherical- and chromatic-aberration corrected SALVE (Sub-Ångström Low-Voltage Electron microscopy) instrument⁹. We work at an electron acceleration voltage of 80 kV, just below the threshold for knock-on damage of C atoms in graphene¹⁴. Under these conditions, the instrument delivers sub-ångström resolution in the images. Further details can be found in Methods (and also in Extended Data Figs. 1, 2).

Figure 2a shows a TEM image of pristine bilayer graphene. The inset depicts its Fourier transform and confirms the known value of the in-plane lattice constant $a_C = 2.46\ \text{Å}$. The image marks the beginning of a series acquired during lithiation of a bilayer graphene device (Fig. 2a–c and Supplementary Video 1), but it is representative of the sample state before application of the bias voltage $U_G = 5\ \text{V}$. In Fig. 2b, acquired after 170 s, a second crystal lattice has appeared in the lower half of the probed area. White dashed lines demarcate its boundary on the left and right of the image. The image in Fig. 2c is recorded at $t = 288\ \text{s}$. The additional crystal structure now extends throughout almost the whole field of view. Figure 2d is the Fourier transform of Fig. 2b. When we compare Fig. 2d with the Fourier transform of pristine bilayer graphene (Fig. 2a inset), we identify three sets of additional signals, highlighted in red, green and blue. These attest to hexagonal crystalline order (as for graphene), but with an in-plane lattice constant of $3.1\ \text{Å}$. In Fig. 2e, the spatial distribution of these additional signals is mapped. This allows three grains to be discerned, none of which are aligned with the encapsulating graphene lattice. In Fig. 2f the same Fourier transform is shown but with a von Hann filter applied to minimize the streaks. The highlighted signals stem from both bilayer graphene (cyan) and the additional crystalline phase (green) as well as moiré artefacts (magenta) and their origin (bold arrows). Figure 2g is a Fourier-filtered (Methods and Extended Data Fig. 3) version of Fig. 2b, where the graphene lattice, as well as the moiré effects, have been removed (see Fig. 2h, i, respectively, for a magnified view before and after filtering). These images offer a direct view of the encapsulated crystal. The observed contrast in the images also suggests regions of different thickness even within a single grain. This is worked out in detail in Methods and Extended Data Fig. 4.

¹Max Planck Institute for Solid State Research, Stuttgart, Germany. ²Materialwissenschaftliche Elektronenmikroskopie, Universität Ulm, Ulm, Germany. ³Institute of Ion Beam Physics and Materials Research, Helmholtz-Zentrum Dresden-Rossendorf, Dresden, Germany. ⁴Department of Applied Physics, Aalto University, Aalto, Finland. ⁵National University of Science and Technology MISiS, Moscow, Russia. ⁶Present address: Department of Chemical Engineering, Massachusetts Institute of Technology, Cambridge, MA, USA. ⁷Present address: Heraeus Battery Technology, Hanau, Germany. ⁸These authors contributed equally: M. Kühne, F. Börrnert. *e-mail: ute.kaiser@uni-ulm.de; j.smet@fkf.mpg.de

To narrow down the chemical composition of the additional crystal structure, electron energy-loss spectroscopy (EELS) data has been acquired on bilayer graphene before and during lithiation (Fig. 2j). Before lithiation ('pristine'), we exclusively observe the C K-edge at 284 eV. During lithiation, the Li K-edge at 55 eV is additionally detected from regions characterized by a Fourier transform like that shown in Fig. 2d. On the basis of the absence of other signals in the explored energy range of 0–800 eV—namely, Si ($L_{2,3}$ -edge at 99 eV), S ($L_{2,3}$ -edge at 165 eV), N (K-edge at 400 eV), O (K-edge at 532 eV and F (K-edge at 685 eV)—we discarded those elements as principal constituents of the new crystalline phase. Likewise, Ti and Pt (electrode material) can be ruled out in view of the observed light atomic contrast in Fig. 2 for the case of Pt and the absence of the distinct Ti $L_{2,3}$ -edge at 456 eV in the EELS data. Although it is inherently impossible to exclude H or C, the crystalline phase formed during lithiation is likely to consist of pure Li. The low onset in the energy of the Li K-edge supports this assertion^{15,16}. Also, a Li plasmon mode^{17,18} appears near 9 eV (Extended Data Fig. 5a). Though the shape of the Li-K edge^{15,16} resembles that of $\text{Li}_2\text{O}/\text{LiOH}$, stoichiometric $\text{Li}_2\text{O}/\text{LiOH}$ can be disqualified, since we would then expect both a more pronounced O-K edge and an imaging contrast comparable in strength to the encapsulating graphene¹⁹. Good agreement with experiment is attained when calculating the Li-K edge shape of graphene-encapsulated Li multilayers (Methods and Extended Data Fig. 5b). We do not rule out the presence of trace oxygen, also suggested by the occasional observation of a weak shoulder near 30 eV (Extended Data Fig. 5a), previously attributed to oxidized lithium^{17,18}. Yet, the extracted in-plane lattice constant of 3.1 Å matches that²⁰ of close-packed Li. This coincidence is surprising, since normally very low temperatures and/or extreme pressures are required for Li to assume this superdense ordering²¹.

To test whether formation of a dense, multi-layered Li crystal in bilayer graphene is conceivable, first-principles calculations were carried out (Methods). The chemical potential of Li atoms in bulk close-packed phases was evaluated. All energies below are given with respect to the hexagonal close-packed (h.c.p.) phase, which had the lowest energy in the calculations. Several layers of Li atoms inside bilayer graphene are considered (Fig. 3 and Extended Data Figs. 6–8). Because the in situ TEM studies do not reveal evidence for a change in registry of the graphene sheets (Extended Data Fig. 9), AB stacking is assumed as in the pristine device. Our main conclusions, however, hold irrespective of the stacking order. The relaxation of atomic coordinates of a single layer of Li atoms yields an energetically favoured C_6LiC_6 configuration, with Li arranged in a commensurate $(\sqrt{3} \times \sqrt{3})\text{R}30^\circ$ superstructure with a lattice constant of $a_{\text{LiC}_6} = 4.26$ Å (Fig. 3a, b). Except for the graphene registry, this finding is similar to the bulk LiC_6 phase¹⁰ that forms in graphite and the AA-stacked C_6LiC_6 phase²². The situation changes for a larger number of Li layers. Finite clusters and infinite (periodic) h.c.p. structures with different orientation with respect to the graphene lattice were considered (Fig. 3c–f, Extended Data Figs. 7, 8). The energies of these systems are very close to that of the C_6LiC_6 configuration (higher by only 0.01–0.05 eV per Li atom). The in-plane lattice constant a_{Li} of the Li h.c.p. bilayer and trilayer (average distances, as the positions of Li atoms are affected by nearby C atoms) is in the range 3.05–3.15 Å, matching the experimental value of 3.1 Å as well as the identical literature value²⁰. These results suggest that the formation of a multilayer close-packed Li phase between graphene sheets is conceivable. Its precise stacking order may, however, differ from h.c.p. as other configurations are energetically similar (Extended Data Fig. 8d, e). These are hard to distinguish in TEM experiments, because we usually only observe the projection along one crystal direction. Moreover, bulk diffraction selection rules do not hold in the given case of an atomically thin specimen. TEM image simulations reveal comparable contrast and diffraction patterns for the two extreme cases: cubic close-packed (c.c.p.) and h.c.p. phases (Extended Data Fig. 2f, g).

By analysing the electronic structure and charge distribution, the charge transfer between Li and graphene can be estimated. Figure 3b, d, f

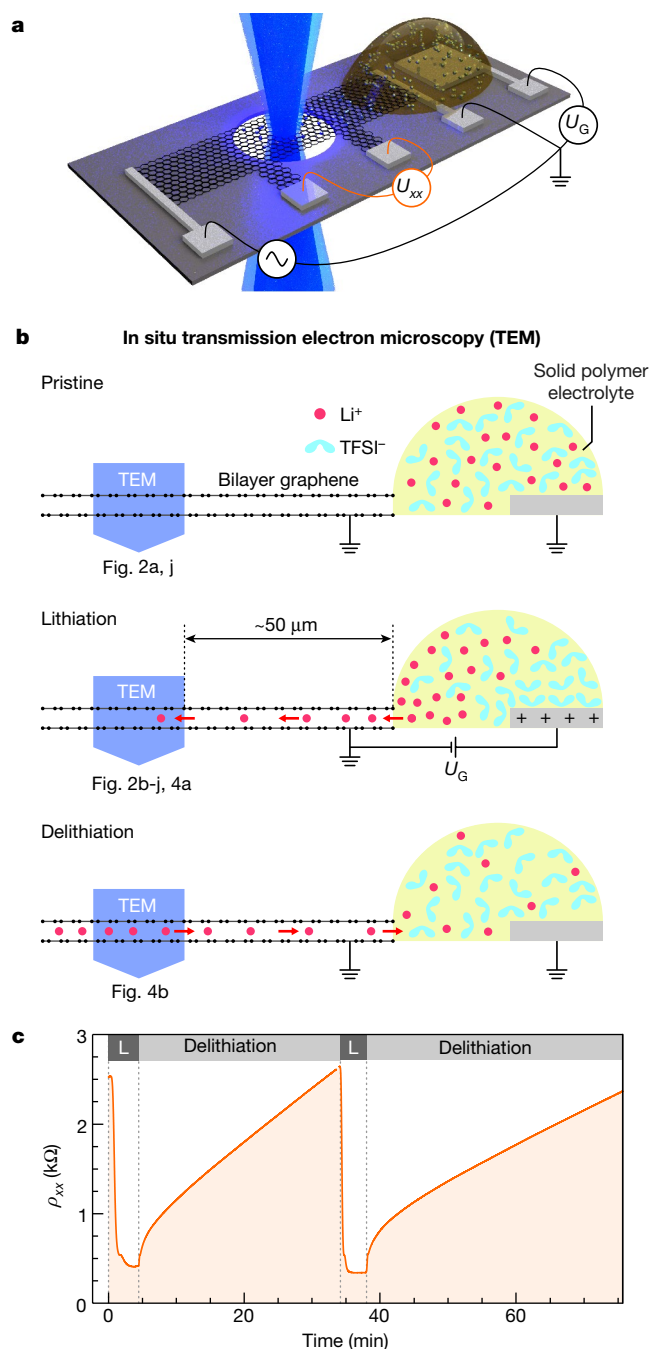


Fig. 1 | Device layout and working principle. **a**, Schematic of the device (not to scale). Bilayer graphene (black) on a Si_3N_4 -covered Si substrate (dark grey) with a membrane at the centre of the chip is contacted by several metallic electrodes (light grey). On the right, a Li-ion (white spheres) conducting electrolyte (yellow) connects the bilayer to a metallic counter electrode to form an electrochemical cell. About 50 μm away from its electrolyte-covered end, bilayer graphene is partially suspended over a hole in the Si_3N_4 , supported by the Si substrate, allowing transmission electron microscopy (TEM) investigations (electron beam illustrated in blue). **b**, Schematic side view of the device during in situ TEM: top panel, the pristine device; middle and bottom panels, the device during lithiation ($U_G = 5$ V at the counter electrode) and delithiation ($U_G = 0$ V), respectively. Ionic components of the solid polymer electrolyte are indicated by red dots and cyan shapes; see Methods for details. Reference to TEM data acquired at the respective state is given. **c**, Bilayer graphene's resistivity ρ_{xx} measured in situ during two lithiation (L)/delithiation cycles inside the SALVE microscope with the electron beam blanked. As schematically shown in **a**, a four-point probe configuration is used to imprint a small a.c. current (—) and measure the local voltage drop U_{xx} in the electrolyte-uncovered region of the device.

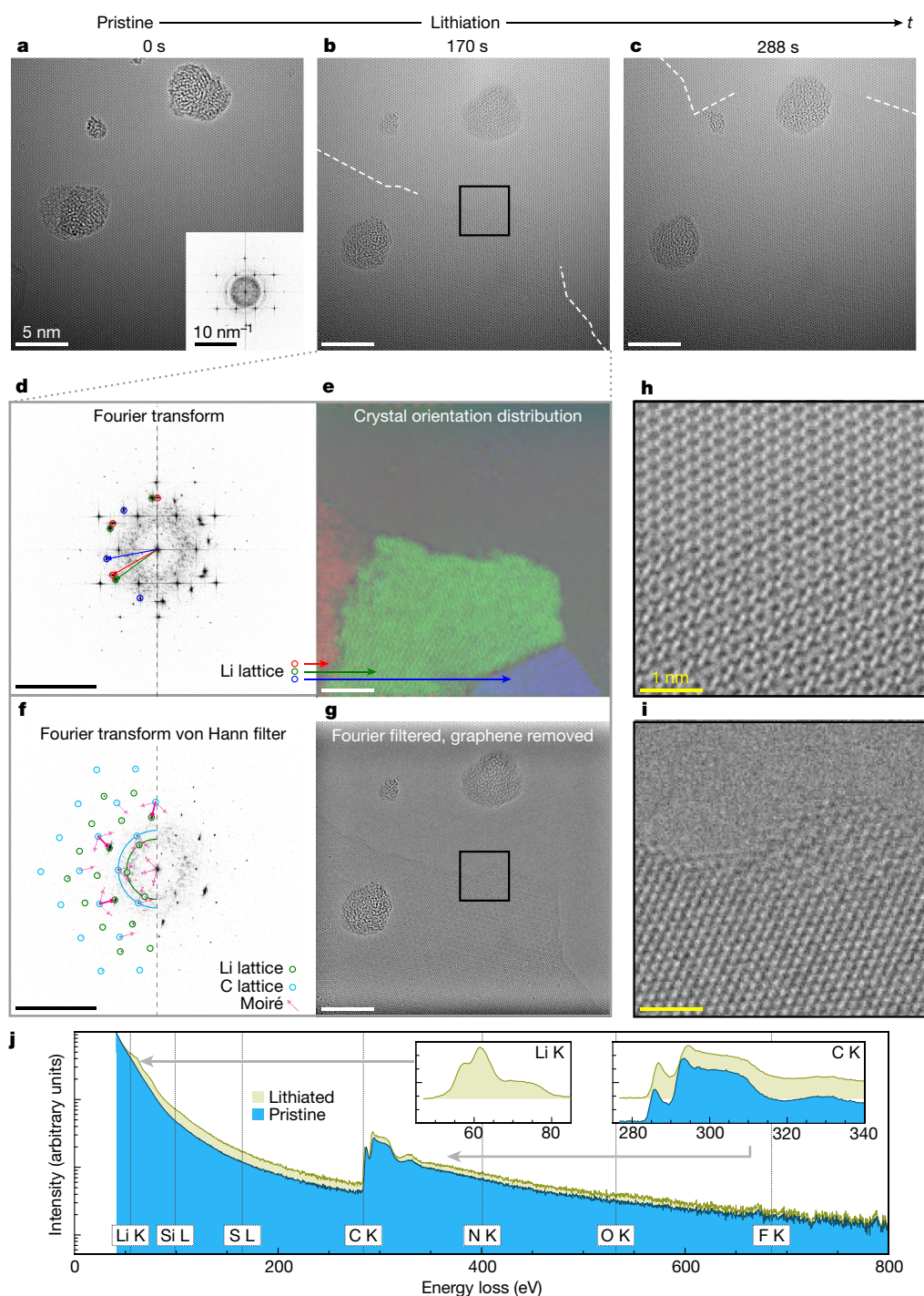


Fig. 2 | In situ TEM measurements. **a–c**, TEM images showing the propagating front (dashed white line) of a Li crystal forming inside bilayer graphene during lithiation. The images are acquired on the same sample area at consecutive times, as indicated at the top. Amorphous hydrocarbon adsorbates appear as blobs a few nanometres wide, located above or below the bilayer. The inset in **a** is its Fourier transform. Panels **d–g** give further information about panel **b**. **d**, Fourier transform of **b**. Three sets of spots marked in red, green and blue are rotated relative to each other as they stem from three different Li crystal grains. The cross-shaped streaks are edge artefacts from the Fourier transform. **e**, Spatial distribution of the Li grains in **b** using the colour coding from **d**. **f**, von Hann-filtered Fourier transform of **b**. Fourier transforms are point-symmetric, therefore, marks on the left side do not mask information. Signals from bilayer graphene (Li) are highlighted in cyan (green); the origins of moiré artefacts are highlighted in bold magenta. The anisotropic smearing of the Li signals is due to the sharp propagation front. Signals originating from the grains

coloured red and blue in **e** are damped away by the applied von Hann filter. Half circles represent the fundamental periodicities of 0.213 nm for graphene (cyan) and 0.276 nm for Li (green). **g**, Fourier-filtered version of **b**, where the graphene lattice, as well as the moiré effects, are filtered out and only the Li crystal structure is left. The contrast at the edge of the figure is an artefact from the Fourier filter. **h**, **i**, Magnified detail from the boxed areas in **b** and **g**, respectively, showing the Li crystal edge. Scale bars of equal size are coloured identically but labelled only once in **a–i**. **j**, EELS data with logarithmic intensity scale before (blue) and during (yellow) lithiation, acquired on an area as in **a** and **c**, respectively. Highlighted are the energies of the relevant major edges. Insets show the near-edge structure of the Li and C K-edges on a linear intensity scale and after individual subtraction of an inverse-power-law background. Note that EELS data become noisy at high energies because of the exponential decay of the signal.

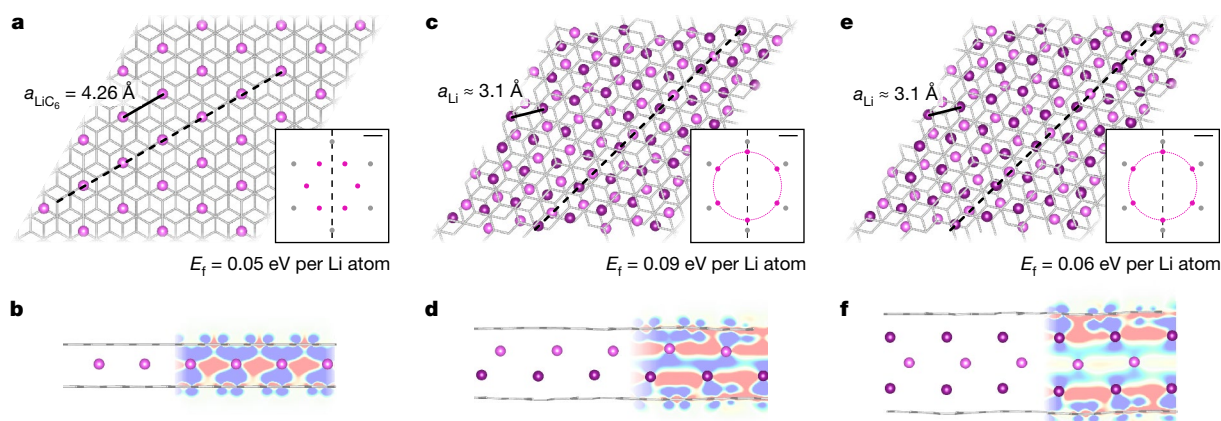


Fig. 3 | Atomistic models of Li crystals between AB-stacked graphene sheets obtained from DFT calculations. a, b, The ‘conventional’ C_6LiC_6 configuration with Li arranged in a commensurate $(\sqrt{3} \times \sqrt{3})R30^\circ$ superstructure between graphene sheets. **c, d,** Fully optimized bilayer Li crystal. **e, f,** Fully optimized trilayer Li crystal (one of two energetically close stacking configurations; compare with Extended Data Fig. 8d). The projection of the latter two structures matches the experimental observations well. Panels **a, c, e** are top views, and panels **b, d, f** are side views along the dashed line given in the respective top view. C atoms and sp^2 bonds are grey, Li atoms are magenta. Solid black lines indicate the in-plane lattice constants of the Li crystals. The insets in **a, c, e** schematically show diffraction patterns associated with the respective structure (scale

bars, 2 nm^{-1}), with first-order diffraction spots from the Li (C) lattice indicated in magenta (grey). The close-packed Li phase in **c, e** may assume any relative rotation angle with respect to the bilayer graphene lattice at virtually no additional energy cost (Extended Data Fig. 7b). A faint magenta circle indicates that the Li diffraction spots may therefore be rotated with respect to those of graphene. E_f is the energy required to take a Li atom from a bulk Li crystal and insert it between graphene sheets in the corresponding configuration. Contour plots in **b, d, f** represent the charge transfer between Li and graphene as compared to the isolated graphene and Li crystals. An increase in the electron density (negative charge) is shown blue, and a decrease in the electron density (positive charge) is shown red.

displays colour renditions of the charge probability distribution as compared to isolated graphene and Li crystals consisting of a single, double or triple layer. As can be seen from Fig. 3f in the triple layer case, charge transfer is noticeable only for the outer Li layers directly neighbouring a graphene sheet. Inner Li layers retain their metallic character as electronic charge is distributed between the Li^+ lattice sites. Extended Data Fig. 8c depicts the average charge transfer per Li atom, which drops as the close-packed Li phase gets thicker. Renormalizing by the number of atoms in the outermost Li layers only, we find a constant charge transfer of approximately $0.33 e^-$ per outer Li atom, irrespective of how many (metallic) Li layers (with nearly zero charge transfer) are packed in between. This is consistent with the observation that the resistivity ρ_{xx} measured during lithiation tends to saturate rather than to decrease progressively as more Li enters bilayer graphene (Fig. 1c). Note that although for C_6LiC_6 (Fig. 3a, b) a higher value of $0.85 e^-$ per Li atom for the charge transfer applies (resulting in an estimated density of transferred electrons of $2.7 \times 10^{14} \text{ cm}^{-2}$ per graphene sheet), the much denser arrangement of Li atoms in the close-packed structure yields a higher electron density per graphene sheet ($4 \times 10^{14} \text{ cm}^{-2}$) despite the smaller charge transfer value.

During lithiation, the close-packed Li phase grows laterally between the graphene sheets (Fig. 4a and Supplementary Video 1). Figure 4a displays a series of digital dark-field versions of the original images, where the three grains of varying in-plane orientation have each been coloured differently. Whereas the grain boundary between the central grain (green) and the lower right grain (blue) is rather sharp and stable, the boundary with the left grain (red) appears more fuzzy and mobile as their orientations nearly match. Regions of different thickness can be identified even within a single grain (Extended Data Fig. 4). The specimen is too thin to allow reliable extraction of its exact thickness t_{Li} from EELS (we typically obtain $t_{Li}/\lambda < 0.1$, where λ is the inelastic mean free path of about 125 nm for 80 keV electrons), but one may nonetheless determine relative variations (see Methods). When imaging an extremely thin slab of weakly scattering elements in a microscope with sufficient resolving power, the imaging contrast increases with increasing specimen thickness. This is quantified in Extended Data Fig. 4e, f, revealing that thinner parts of the close-packed Li phase tend to be located closer to its perimeter. At the leading edge, single atoms can be identified

(Methods, Extended Data Fig. 1). From the image time series, a lateral growth rate of the order of 1 \AA s^{-1} can be extracted. During delithiation, the close-packed Li phase disassembles and gradually disappears (Fig. 4b). Eventually, the pure bilayer graphene lattice remains behind. The degree of reversibility of this process is limited by the number of defects in the graphene lattice and their irreversible formation during prolonged imaging (electron irradiation). Given the combination of slow image acquisition (of the order of 1 s) and low sensitivity to light atoms, rapid diffusion of single Li ions that are not ordered remains concealed from the TEM observer. It is nonetheless present, both within and beyond the superdense phase, and is likely to be responsible for the initial abrupt change in resistivity ρ_{xx} during lithiation (Fig. 1c).

We note that the observed crystalline phase of Li proves stable only between intact graphene planes. When the incident electron energy exceeds the threshold for displacement damage of Li (about 20 keV), conditions are such that Li readily ‘boils’ under the electron beam^{16,18}. The close-packed phase is volatile when imaged near bilayer edges or in the presence of a high density of defects in the graphene lattice. Constituents may escape from between graphene sheets via such edges or defects on electron-beam-induced melting of the crystalline phase. Likewise, we find that material having escaped from within and agglomerated on the outer bilayer surfaces near such defects quickly evaporates under electron beam irradiation. The protective encapsulation by two impermeable atomic sheets may thus be regarded a prerequisite for safe probing by TEM of the crystal formation therein, akin to the situation in graphene liquid cells²³.

Close-packing of Li intercalated between graphene sheets, as demonstrated here, results in a structure with a Li content greatly in excess of LiC_6 . Although enhanced Li storage has been previously proposed to occur on the outside of graphene planes^{24,25}, the suggested atomistic configurations were contradictory and could neither be addressed nor verified by microscopic means. Other reports claiming the formation of nanocrystallites of close-packed Li during the lithiation of different carbon allotropes are scarce and not fully consistent^{26,27}. At elevated temperatures, a configuration of Li similar to that which we report here may have been left unidentified in bulk graphite²⁸.

Because the energy cost for close-packing of Li in the van der Waals gap of bilayer graphene is very similar to that of forming C_6LiC_6

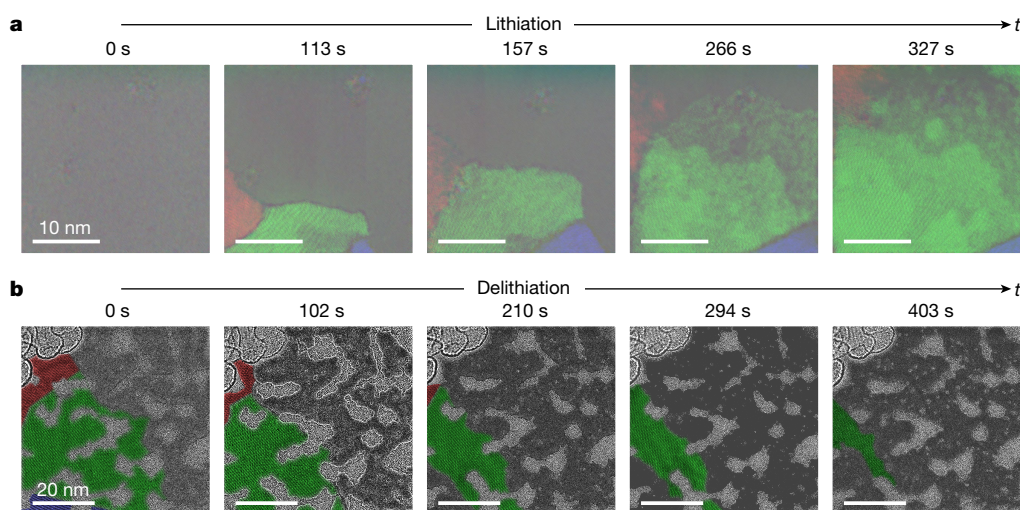


Fig. 4 | Li crystal growth between two graphene sheets. a, b, Time series of digital dark-field versions of the original images during lithiation (**a**) and (**b**) delithiation; times are shown at top of panels. Crystal grains of different in-plane orientation are coloured in red, green and blue. An increased amount of amorphous, immobilized residues (grey areas,

essentially composed of carbon) are present within the field of view in **b**, an unavoidable consequence of extended electron beam illumination. In both **a** and **b** the interface with the electrolyte (not contained in the images) is oriented towards the bottom of the page.

(Fig. 3), close-packing may be the way the system accommodates a large amount of Li supplied within a short time. The activation energy for Li diffusion in bilayer graphene has been calculated (Methods, Extended Data Fig. 10). It points towards facile diffusion of Li between graphene sheets by the exchange mechanism, even in the presence of a close-packed Li phase. And although a graphene bilayer can be regarded as the structural unit of thicker graphite, its properties differ in many respects. Two atomic sheets may well spread more easily when isolated from their bulk crystal and thus render new types of intercalate ordering possible. Even if so, the stabilization of a superdense lithium phase comes as a surprise as its appearance has typically been reserved for extreme conditions²¹ only. It is noteworthy that Li–graphite intercalation compounds only occupy a small region of the C–Li binary alloy phase diagram²⁹. In the miscibility gap beyond LiC_6 , alternative configurations may be available for storing larger amounts of lithium in layered carbons³⁰.

Online content

Any methods, additional references, Nature Research reporting summaries, source data, statements of data availability and associated accession codes are available at <https://doi.org/10.1038/s41586-018-0754-2>.

Received: 8 January; Accepted: 15 October 2018;

Published online: 26 November 2018

- Winter, M. & Besenhard, J. O. In *Handbook of Battery Materials* 2nd edn (eds Daniel, C. & Besenhard, J. O.) 433–478 (Wiley-VCH, Weinheim, 2011).
- Kaskhedikar, N. A. & Maier, J. Lithium storage in carbon nanostructures. *Adv. Mater.* **21**, 2664–2680 (2009).
- Zheng, H., Meng, Y. S. & Zhu, Y. Frontiers of in situ electron microscopy. *MRS Bull.* **40**, 12–18 (2015).
- Qian, D., Ma, C., More, K. L., Meng, Y. S. & Chi, M. Advanced analytical electron microscopy for lithium-ion batteries. *NPG Asia Mater.* **7**, e193 (2015).
- Liu, X. H. et al. In situ TEM experiments of electrochemical lithiation and delithiation of individual nanostructures. *Adv. Energy Mater.* **2**, 722–741 (2012).
- Shao-Horn, Y., Croguennec, L., Delmas, C., Nelson, E. C. & O’Keefe, M. A. Atomic resolution of lithium ions in LiCoO_2 . *Nat. Mater.* **2**, 464–467 (2003).
- Oshima, Y. & Murakami, Y. (eds) *Microscopy* **66** (Challenges for Lithium Detection special issue), 1–61 (2017).
- Reimer, L. & Kohl, H. *Transmission Electron Microscopy* (Springer Series in Optical Sciences, Springer, New York, 2008).
- Linck, M. et al. Chromatic aberration correction for atomic resolution TEM imaging from 20 to 80 kV. *Phys. Rev. Lett.* **117**, 076101 (2016).
- Enoki, T., Suzuki, M. & Endo, M. *Graphite Intercalation Compounds and Applications* (Oxford Univ. Press, New York, 2003).
- Yu, Y. et al. Gate-tunable phase transitions in thin flakes of 1T-TaS₂. *Nat. Nanotechnol.* **10**, 270–276 (2015).
- Bediako, D. K. et al. Heterointerface effects in the electrointercalation of van der Waals heterostructures. *Nature* **558**, 425–429 (2018).
- Kühne, M. et al. Ultrafast lithium diffusion in bilayer graphene. *Nat. Nanotechnol.* **12**, 895–900 (2017).
- Meyer, J. C. et al. Accurate measurement of electron beam induced displacement cross sections for single-layer graphene. *Phys. Rev. Lett.* **108**, 196102 (2012).
- Mauchamp, V., Boucher, F., Ouvrand, G. & Moreau, P. Ab initio simulation of the electron energy-loss near-edge structures at the Li K edge in Li, Li₂O, and LiMn₂O₄. *Phys. Rev. B* **74**, 115106 (2006).
- Wang, F. et al. Chemical distribution and bonding of lithium in intercalated graphite: identification with optimized electron energy loss spectroscopy. *ACS Nano* **5**, 1190–1197 (2011).
- Lru, D.-R. & Williams, D. B. The electron-energy-loss spectrum of lithium metal. *Phil. Mag. B* **53**, L123–L128 (1986).
- Hightower, A., Ahn, C. C., Fultz, B. & Rez, P. Electron energy-loss spectrometry on lithiated graphite. *Appl. Phys. Lett.* **77**, 238–240 (2000).
- Liu, X. H. et al. In situ transmission electron microscopy of electrochemical lithiation, delithiation and deformation of individual graphene nanoribbons. *Carbon* **50**, 3836–3844 (2012).
- Wyckoff, R. W. G. *Crystal Structures* Vol. 1, 2nd edn (Wiley & Sons, 1963).
- Ackland, G. J. et al. Quantum and isotope effects in lithium metal. *Science* **356**, 1254–1259 (2017).
- Sugawara, K., Kanetani, K., Sato, R. & Takahashi, T. Fabrication of Li-intercalated bilayer graphene. *AIP Adv.* **1**, 022103 (2011).
- Yuk, J. M. et al. High-resolution EM of colloidal nanocrystal growth using graphene liquid cells. *Science* **336**, 61–64 (2012).
- Sato, K., Noguchi, M., Demachi, A., Oki, N. & Endo, M. A mechanism of lithium storage in disordered carbons. *Science* **264**, 556–558 (1994).
- Deschamps, M. & Yazami, R. Great reversible capacity of carbon lithium electrode in solid polymer electrolyte. *J. Power Sources* **68**, 236–238 (1997).
- Wang, Q. et al. Investigation of lithium storage in bamboo-like CNTs by HRTEM. *J. Electrochem. Soc.* **150**, A1281–A1286 (2003).
- Lee, B.-S. et al. Face-centered-cubic lithium crystals formed in mesopores of carbon nanofiber electrodes. *ACS Nano* **7**, 5801–5807 (2013).
- Kambe, N. et al. Intercalate ordering in first stage graphite-lithium. *Mater. Sci. Eng.* **40**, 1–4 (1979).
- Okamoto, H. In *Binary Alloy Phase Diagrams* Vol. 1, 2nd edn (eds Massalski, T. B., Okamoto, H., Subramanian, P. R. & Kacprzak, L.) **857** (ASM International, Ohio, 1990).
- Lin, D. et al. Layered reduced graphene oxide with nanoscale interlayer gaps as a stable host for lithium metal anodes. *Nat. Nanotechnol.* **11**, 626–632 (2016).

Acknowledgements We acknowledge financial support from the Baden-Württemberg Stiftung gGmbH (project CT 5) and from the European Union Graphene Flagship. We are grateful to FEI/ThermoFisher Scientific for providing drawings and specifications of the NanoEx-i/v holder. F.B., J.B. and U.K. acknowledge funding from the German Research Foundation (DFG) and the Ministry of Science, Research and the Arts (MWK) of the federal state of Baden-Württemberg, Germany, in the frame of the SALVE project. A.V.K. thanks the Academy of Finland for support under project number 286279 and the DFG under project KR 4866/1-1. The theoretical study of Li diffusion (A.V.K.) was supported by the Russian Science Foundation (project identifier, 17-72-20223). We thank K. v. Klitzing for discussions and support and J. Popovic

for useful comments on the manuscript. We acknowledge CSC Finland and PRACE (HLRS, Stuttgart, Germany) for generous grants of CPU time.

Reviewer information *Nature* thanks I. Honma and the other anonymous reviewer(s) for their contribution to the peer review of this work.

Author contributions J.H.S. and U.K. composed the project. M.K. and S.F. fabricated samples and performed electrochemical measurements. F.B. performed the TEM and EELS experiments. M.G. and A.V.K. did the DFT calculations. J.B. helped with TEM and EELS experiments and did TEM imaging simulations. U.K. supervised the TEM work. D.S. contributed to the electrochemical design of the experiment. M.K. and J.H.S. wrote the manuscript and all authors contributed to it.

Competing interests The authors declare no competing interests.

Additional information

Extended data is available for this paper at <https://doi.org/10.1038/s41586-018-0754-2>.

Supplementary information is available for this paper at <https://doi.org/10.1038/s41586-018-0754-2>.

Reprints and permissions information is available at <http://www.nature.com/reprints>.

Correspondence and requests for materials should be addressed to U.K. or J.H.S.

Publisher's note: Springer Nature remains neutral with regard to jurisdictional claims in published maps and institutional affiliations.

METHODS

Sample fabrication. Bulk natural graphite (NGS Naturgraphit) was exfoliated using adhesive tape³¹ onto a sacrificial poly(methyl methacrylate) (PMMA) layer. A suitable bilayer graphene flake was selected with the help of an optical microscope. From the characteristic Raman scattering response, its bilayer nature³² was verified. Using a dry-transfer method³³, the bilayer was placed over a hole in the Si₃N₄ membrane of a custom-made TEM sample carrier chip. A PMMA mask was patterned using electron-beam lithography followed by O₂-plasma etching in order to shape and isolate the desired flake. Multiple electrical contacts to the bilayer as well as the counter electrode were realized by standard lift-off techniques. In this work, samples with contacts made of either 60-nm-thick evaporated Ti or 60-nm-thick sputter-deposited Pt were used. The devices were annealed at 300 °C in a low-pressure (about 150 mbar) forming gas atmosphere. Inside an Ar-filled glovebox, 0.35 M lithium bis(trifluoromethane) sulfonimide (Li-TFSI) in polyethylene glycol methyl ether methacrylate:bisphenol A ethoxylate dimethacrylate (m-PEGMA:BEMA) w/w 3:7 electrolyte with added 2–4 wt% of 2-hydroxy-2-methylpropiophenone (HMPP) as photoinitiator was drop-casted on each sample, assuring only partial coverage of bilayer graphene (such that the sample area on the hole remained uncovered) and connecting it with the counter electrode. The electrolyte (see further details elsewhere^{13,34}) was cured under ultraviolet radiation and capped by 200 nm evaporated SiO_x to prevent outgassing.

In situ TEM measurements. Measurements were performed inside the SALVE transmission electron microscope (see also <http://www.salve-project.de>) consisting of an FEI Titan Themis³ column fitted with a CEOS aberration corrector. The corrector is a quadrupole-octupole corrector of modified Rose-Kuhn design that corrects for first order chromatic aberrations, fifth order axial geometric aberrations, and third order off-axial geometric aberrations⁹. The electron source is an FEI X-FEG Schottky type and the camera used is an FEI CETA 16M fibre coupled CMOS camera. Images were acquired using exposure times of 1 s at electron dose rates of about $(2\text{--}5) \times 10^6 \text{ e}^- \text{ nm}^{-2} \text{ s}^{-1}$ (4,096 by 4,096 pixels per frame). The camera pixel size at the magnification chosen for the lithiation time series was $(6.9 \text{ pm})^2$ at an optical resolution of 70 pm. Local EELS spectra were taken with a Gatan Quantum ERS energy filter attached to the microscope. The microscope was operated at an electron acceleration voltage of 80 kV. From the full-width at half-maximum (FWHM) of the zero-loss peak we determine an energy resolution of about 0.7 eV. The sample space is kept at a base pressure of $p = 10^{-7}$ mbar, with the sample itself immersed in a static magnetic field of $B = 1.4$ T. We use an FEI NanoEx-i/v holder, providing eight electric feed-throughs to the sample using custom-made sample chip carriers. Four-terminal measurements of the electronic transport properties of uncovered bilayer graphene were done in situ using conventional lock-in techniques, with a low-frequency (13.33 Hz) a.c. excitation current of $I = 100$ nA applied across the bilayer. Lithiation (delithiation) was induced by applying a constant voltage $U_G = 5$ V ($U_G = 0$ V) to the metallic counter electrode using a source-measure unit. For atomic-resolution imaging, the graphene bilayer was cleaned in situ by current annealing³⁵ before the first lithiation. All experiments were performed at room temperature, with the sample exposed to the high vacuum environment of the transmission electron microscope.

TEM imaging resolution. The optical resolving power of the SALVE instrument⁹, operated at 80 kV, is better than 0.08 nm. However, the true image resolution is element-specific, governed by the (scattering-angle-dependent) differential scattering cross-section. Li being a light element, its differential cross-section for scattering into high angles is small. Yet high-angle scattering is important for achieving high image resolution. In the Fourier transforms shown in Fig. 2a, d, f, one sees signals from the C lattice up to $(71 \text{ pm})^{-1}$, indicating a nonlinear information transfer up to at least 0.07 nm. The highest Li lattice frequency in Fig. 2d, f is $(90 \text{ pm})^{-1}$, indicating a nonlinear information transfer up to at least 0.09 nm. If we were imaging a strong scatterer or a thick specimen in a conventional C_s-corrected microscope, a conservative estimate for the upper limit of the linear information transfer (that determines the real imaging resolution) would be given by half the value of the highest observed frequency, that is, 0.14 nm for C and 0.18 nm for Li. However, first of all, we are dealing with an extremely weak scatterer and the sample is very thin, even in the context of TEM. Thus, the nonlinear information transfer portion is small. Second, the instrument used is chromatic-aberration-corrected in addition to the geometric aberration correction. Unlike in a C_s-only corrected microscope, the nonlinear information transfer is dampened in approximately the same way as the linear information transfer³⁶. For these two reasons, our real imaging resolution in fact closely corresponds to the value of the highest frequency in the Fourier transforms, that is, about 0.07 nm for C and 0.09 nm for Li. These values are not only smaller than the observed in-plane lattice constant $a_{\text{Li}} \approx 3.1$ Å of the close-packed Li phase, but also smaller than the nearest possible distance between the projection (along the *c* axis) of Li atoms located in different layers of this phase, which is about

1.8 Å. They are even smaller than the distance between nearest-neighbouring C atoms in graphene (1.42 Å). True atomic image resolution of the C and Li lattices is therefore achieved.

TEM sensitivity. In our TEM images we may identify individual Li atoms where the crystalline Li phase appears thinnest, that is, at the leading edge. In Extended Data Fig. 1e we highlight single Li atoms, appearing as dark spots at the very front of the growing Li phase. These spots are not due to image delocalization, since they are non-periodic. In the given regime of weakly scattering elements and very few atoms, the image contrast simply adds up. Consequently, the contrast value of a single C atom (atomic number 6) is identical to that of two superposed Li atoms (atomic number 3). Vice versa, the contrast value of a single Li atom corresponds to half the value of a single C atom. By Fourier filtering the TEM images, the information of a perfect bilayer graphene lattice is subtracted from the images. At sites where one C atom is missing in one of the two graphene sheets, this procedure adds the contrast information of a single C atom, which may serve as a reference. Extended Data Fig. 1f, g displays two line profiles of the imaging contrast (Extended Data Fig. 1f left and right): one of these runs across two Li atoms at the leading edge, and the other is centred on such a reference site (Extended Data Fig. 1g left and right). The contrast value of each Li atom is indeed about half that corresponding to one C atom.

Image simulations were carried out using the open-source program QSTEM (<http://qstem.org>). To create atomistic models, standard tools like Materials Studio (Accelrys Inc.) as well as a custom-made program were used. The following simulation parameters determined from the experiments were applied: electron energy $E = 80$ kV, spherical aberration $C_s = -10$ μm, remaining residual focus spread $\Delta F_s = 0.5$ nm, image spread $\Delta I_s = 25$ pm, convergence angle $\alpha = 0.5$ mrad, and applied electron dose $2 \times 10^6 \text{ e}^- \text{ nm}^{-2}$ using Poisson statistics. The focus was used as a free parameter. The SALVE TEM image simulations, summarized in Extended Data Fig. 2a–e, show that the detection limit of the instrument with the imaging parameters used is sufficient to resolve single Li atoms. The bilayer graphene lattice was removed from simulated images by Fourier filtering. Extended Data Fig. 2a, b displays the atomistic model: a hexagonal close-packed Li wedge (red) between two graphene sheets (cyan). To the left of the edge of the Li wedge, five additional Li atom rows were included. Furthermore, several vacancies were introduced to the Li lattice. In panels c–e the corresponding dose-limited TEM image simulations are shown. The Li wedge with graphene above and below does not directly reveal single Li atoms (Extended Data Fig. 2c). However, these atoms become clearly apparent in the filtered image in Extended Data Fig. 2d, as do the vacancies in the Li lattice. To verify the accuracy of the filtering procedure, a dose-limited TEM image simulation of the Li-wedge only, that is, without the graphene lattice (see Extended Data Fig. 2e), was performed. Both the single Li atoms and the vacancies are clearly visible, showing contrast similar to that in the filtered image (Extended Data Fig. 2d).

Fourier filtering. The original images shown in Fig. 2a–c, h are unfiltered; in these, the graphene bilayer lattice is atomically resolved. Additionally, we show images where the graphene lattice and the moiré effects have been filtered away (Fig. 2g, i); we cut out only sharp signals in Fourier space, and the cutout was very local. The signals of the Li phase are not affected at all. Note that neither a bandpass filter nor a Wiener filter was used, as these might have a slight impact on the atom positions. Nor did we use a filter that isolates the Li signals and may additionally enhance the apparent resolution of the image. The exact mask applied in Fourier space and the remaining Fourier transform are illustrated in Extended Data Fig. 3a and b, respectively. The filtered Fourier transform (Extended Data Fig. 3b) of the original image was back-transformed to real space (Fig. 2g). In the filtered Fourier transform (Extended Data Fig. 3b), the streaking (highlighted in yellow) resulting from the edges of the real image is very prominent in every spot. This streaking was not filtered out in order to avoid masking too-large portions of Fourier space. The streaking is responsible for the artefacts at the edges of the filtered image. Finally, the inhomogeneity of the illumination in the original image is gone in the filtered image because the central part of the Fourier transform was also cut out.

One effect of filtering out the bilayer graphene is that effectively a perfect lattice is subtracted from the image. Local defects in the graphene lattice thus become visible in the filtered image. For example, a vacancy in one graphene layer appears as a carbon atom with inverted contrast in the filtered image, as shown in Extended Data Fig. 1f–h.

Thickness determination. The observed close-packed Li phase reveals regions of different thickness. This is illustrated in Extended Data Fig. 4a, where major edges enclosing regions of approximately constant thickness have been marked. The two Fourier transforms identify regions of apparently different thickness but belonging to a single grain. EELS measurements of the Li phase during lithiation of a graphene bilayer have been performed. The 80 keV electron beam was spread over a region of several hundred nm² to minimize the areal dose. EEL spectra have been recorded without apparent detrimental effects of beam exposure on the Li

phase. From the EELS data, we may extract an estimate for the thickness t_{Li} of the Li phase using:

$$\frac{t_{\text{Li}}}{\lambda} = \ln \left(\frac{I_t}{I_0} \right)$$

with I_t the integrated intensity of the total EEL spectrum and I_0 the integrated intensity of the direct beam. The inelastic mean free path $\lambda \approx 125$ nm for 80 keV electrons in Li was determined according to ref. ³⁷. For all EEL spectra acquired on lithiated bilayer graphene, we find $t_{\text{Li}}/\lambda < 0.1$, with typical values of $t_{\text{Li}} \approx 3$ –4 nm. While this finding indeed points to a thin Li phase, it certainly does not represent its true thickness. The described method relies on the assumption that the integrated energy loss stems from bulk excitations, while surface excitations are entirely neglected. In the case at hand however, surface excitations are by far the dominant source of electron energy loss. Also, graphene surface excitations are contained in the spectrum, rendering extraction of information about the Li phase non-trivial. Therefore, the stated value represents an upper bound to the true thickness of the Li phase.

Knowing that the specimens are thin, the electron scattering cross-sections small, and the resolution of the SALVE TEM sufficient, relative variations in thickness of the close-packed Li phase may be determined as follows. Under these conditions, the contrast in the TEM images is expected to increase with increasing specimen thickness. Extended Data Fig. 4e is a reprint of Extended Data Fig. 4a, where green dashed lines demarcate boundaries between regions of approximately constant thickness within a single grain of the observed Li phase. From three regions that display different contrast (i, ii and iii in Extended Data Fig. 4e), we extract the histograms plotted in Extended Data Fig. 4f. The FWHM attests to the respective strength in contrast of these regions. For the conditions of the experiment, the larger the FWHM of the histogram the thicker (locally) the Li phase is. In the given case, the Li phase in region i is thinnest, while in region iii it is thickest.

Extended Data Fig. 2f, g displays SALVE TEM image simulations for Li wedges assuming two different close-packed Li structures: cubic and hexagonal. Extended Data Fig. 2a displays the atomistic models used, both in side view and in top view. The incident 80 keV electron beam is parallel to the normal of the layer planes. The corresponding image simulations are shown in Extended Data Fig. 2g for two different focus values (+6 nm overfocus and –6 nm underfocus; both at Lentzen conditions). Indeed, the tendency of increasing contrast for increasing number of close-packed layers for both systems is confirmed.

Low-loss EELS. Low-loss EELS data were recorded on graphene bilayers both before and during lithiation. Typical spectra are shown in Extended Data Fig. 5a. The dose rates were approximately $5 \times 10^6 \text{ e}^- \text{ nm}^{-2} \text{ s}^{-1}$ and the illuminated area was slightly larger than the imaged area. For the following, the optical mode was switched to diffraction with the central beam entering the entrance aperture of the spectrometer. Typical integration times were 10 s. Upon lithiation, the close-packed Li phase formed between graphene sheets. Concomitant with the Li-K edge, a pronounced new peak appeared in the low-loss region near 9 eV (Extended Data Fig. 5a). A similar feature was reported from EELS measurements on lithium metal and attributed to a Li plasmon mode^{17,18}. We note the occasional observation of a weak shoulder near 30 eV, which can also be seen in Extended Data Fig. 5a. This shoulder has been attributed to oxidized lithium^{17,18} and hence we do not exclude the presence of trace amounts of it within the probed area of the sample.

First-principles calculations. Density functional theory (DFT) calculations were carried out in the plane-wave basis and within the projector-augmented wave description of the core regions, as implemented in the VASP code^{38,39}. The exchange–correlation functional proposed by Perdew, Burke and Ernzerhof⁴⁰ (PBE) and the van der Waals functional suggested by Björkman⁴¹ were adopted for simulations of van der Waals-bonded 2D materials. An energy cut-off of 600 eV was used for the primitive cell calculations. For supercells we used 400 eV and 300 eV for the largest supercell with 624 atoms, corresponding to the 12×12 supercell of C_6LiC_6 . The Brillouin zones of the primitive cell and supercells were sampled using $12 \times 12 \times 12$ (bulk lithium) and $2 \times 2 \times 1$ (2D supercells) Monkhorst–Pack grid points⁴². The maximum force on each atom is set to be less than 0.01 eV for optimized structures. The atomistic structures and the difference charge densities were illustrated using VESTA⁴³.

Various initial configurations of Li atoms between graphene sheets were created, and then the geometry was fully optimized (Extended Data Figs. 6–8). We considered both finite clusters of Li atoms and periodic commensurate Li–graphene systems. In order to reduce the lattice mismatch for periodic structures, the optimum size of the supercell and rotational angles between surfaces was found using the Virtual NanoLab software⁴⁴. Finite Li clusters were encapsulated inside a 12×12 graphene bilayer supercell composed of 576 atoms.

We simulated both AA and AB stacked graphene. The formation energy E_f is obtained from

$$E_f = \frac{E_{\text{graphene+Li}} - E_{\text{graphene}}}{n_{\text{Li}}} - \mu_{\text{Li}}$$

where $E_{\text{graphene+Li}}$ is the energy of the supercell containing bilayer graphene and Li atoms, E_{graphene} is the energy of pristine bilayer graphene, n_{Li} is the total number of Li atoms and μ_{Li} is their chemical potential.

Electron energy loss near edge structure (ELNES). The ELNES simulations were performed using the all-electron full potential linear augmented plane wave (FLAPW) method with the TELNES program⁴⁵ as implemented in the WIEN2k package^{46,47}. The calculations were all done within the generalized gradient approximation (GGA) using PBE exchange and correlation potential. The muffin-tin radii R_{mt} for Li and C atoms are 2.09 and 1.34 atomic units (a.u.), respectively. $R_{\text{mt}}K_{\text{max}}$ was fixed at 7.0 to determine the basis size. The full Brillouin zone was sampled by $5 \times 5 \times 1$ k points. The ELNES spectra were calculated using the double differential scattering cross-section (DDSCS) for the excitation of an atom by fast electrons and is given by the expression:

$$\frac{\partial^2}{\partial E \partial \Omega} = \frac{4\gamma^2}{a_0^2} \frac{k}{k_0} \frac{1}{Q^4} S(Q, E)$$

where a_0 is the Bohr radius, γ is the relativistic factor, k_0 and k are the electron wave vectors before and after interaction, respectively, and $Q = k_0 - k$ is the momentum transfer. In this approximation:

$$S(Q, E) = \sum_{i,f} |\langle i | e^{iQr} | f \rangle|^2 \delta(E + E_i - E_f)$$

for excitations from the initial state $|i\rangle$ with eigenvalue E_i to the final state $|f\rangle$ with eigenvalue E_f . The EELS calculations were performed using actual experimental conditions, such as beam energy, collection semi-angle, beam orientation and a spectrometer broadening of 0.75 eV. For comparison reasons, the simulated spectra were shifted to the major feature of the experimental spectrum (Extended Data Fig. 5b).

Li diffusion in bilayer graphene. In a first step, the diffusion barrier of a single Li atom between graphene sheets was calculated. For simplicity, only the relevant AB stacking configuration was considered. We obtained a barrier of 0.47 eV, in agreement with reported values for Li migration in graphite (0.4–0.6 eV, obtained using similar methods), see for example refs ^{48–51} and references therein.

In a second step, the diffusion barrier for lateral diffusion of a Li atom within two close-packed layers of Li encapsulated between two graphene sheets was calculated. To this end, an extra interstitial Li atom was considered as illustrated in Extended Data Fig. 10. The presence of the neighbouring graphene sheet forces the atom to take a position almost within the Li plane, in the middle of a Li triangle. In reality, the configuration gets distorted due to the interaction with the graphene layer. Note that the extra atom ‘pushes’ away the neighbouring Li atoms to make some space. The extra atom diffuses through the exchange mechanism with the nearest Li atom (see Extended Data Fig. 10c, d). One may think about this diffusion process as the motion of a Li–Li dimer. For its activation, we find a barrier lower than 0.3 eV. In reality, the value should depend on the exact position of the extra Li atom in the moiré pattern and correspondingly on the orientation of the Li lattice with respect to the graphene lattice. However, as the diffusion proceeds within the plane, we do not expect a strong dependence. It thus seems that at room temperature the Li atoms may easily move within the close-packed Li phase.

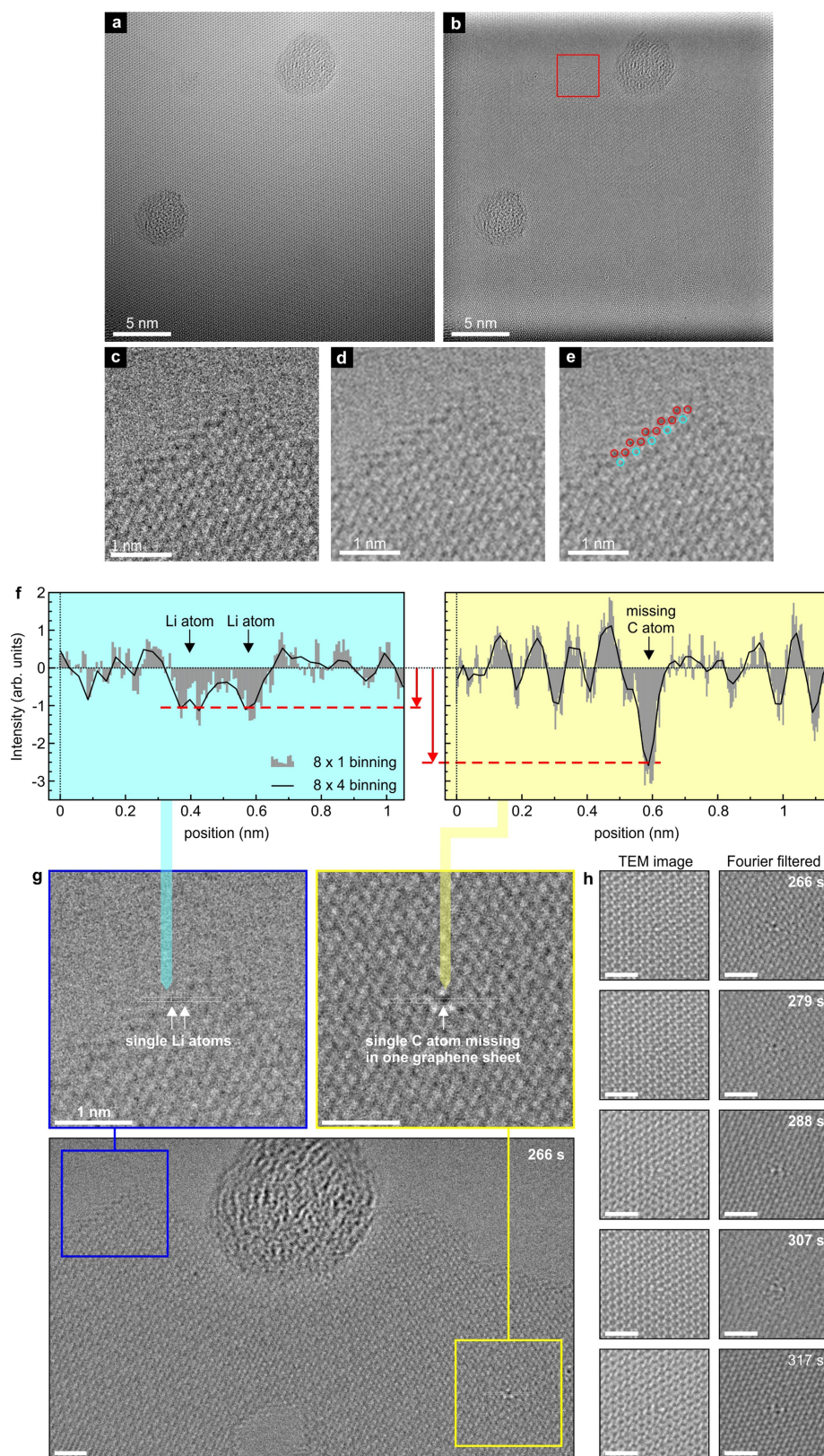
The outside of bilayer graphene in principle offers an alternative pathway for lateral diffusion of Li ions. Followed by vertical diffusion via defect sites, Li ions may thus potentially reach any place between the two graphene sheets. And even though Li diffusion on the outside of graphene sheets is expected to be fast⁵², we did not observe a measurable efficiency of this diffusion pathway in previous work¹³. Despite a low theoretical barrier for Li migration on graphene’s outside⁵¹, of the order of 0.2 eV, it is energetically much more favourable for Li to reside between graphene sheets (the difference being about 0.6 eV). Unlike the case where Li is evaporated first on the outside of graphite followed by rapid lateral diffusion and intercalation⁵², in our case Li ions from the electrolyte intercalate in between the graphene sheets followed by lateral diffusion within the sheets. This has been confirmed in the study in ref. ¹³.

Data availability

The data that support the findings of this study are available from the corresponding authors on request.

- Novoselov, K. S. et al. Electric field effect in atomically thin carbon films. *Science* **306**, 666–669 (2004).

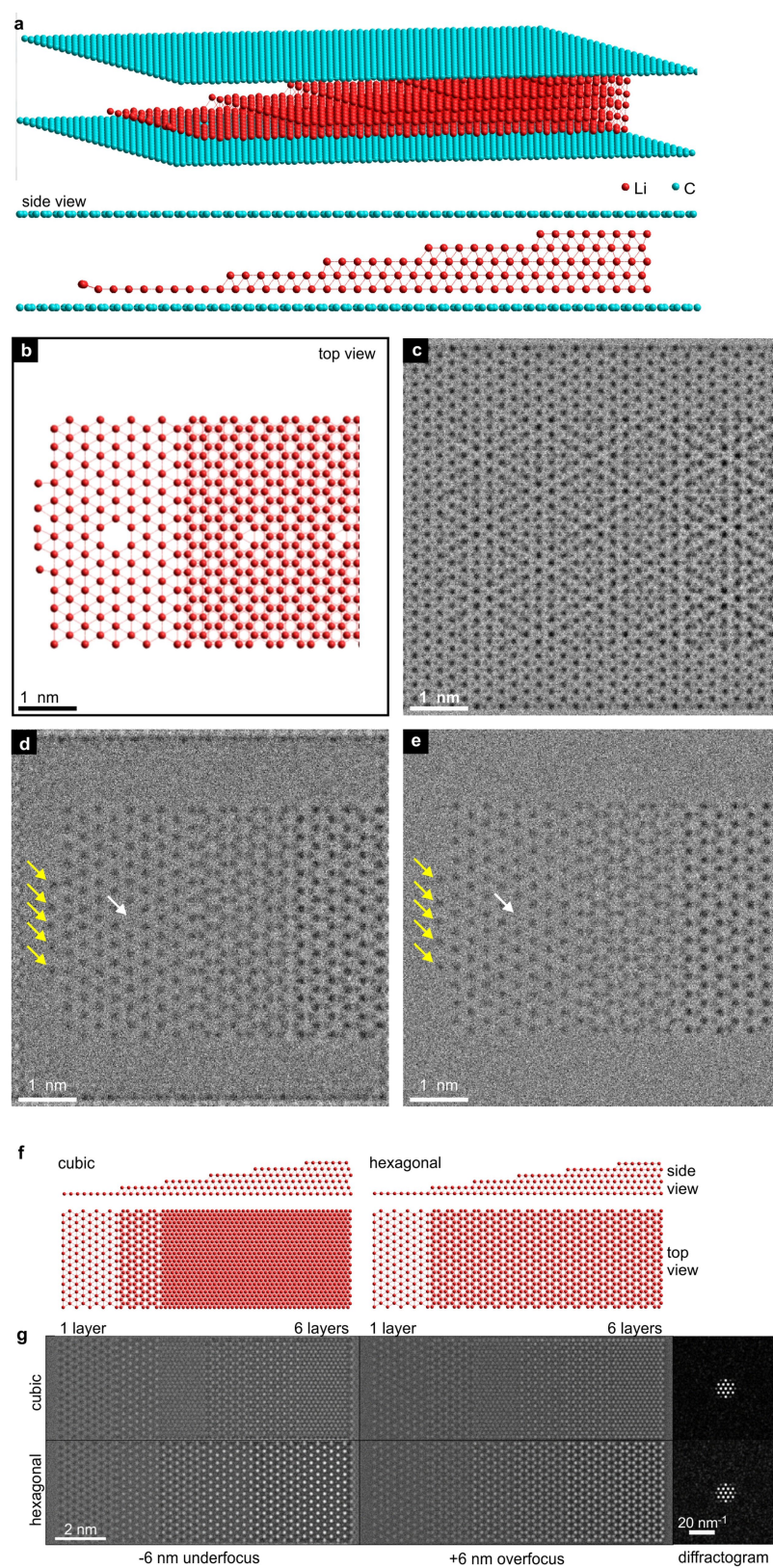
32. Ferrari, A. C. et al. Raman spectrum of graphene and graphene layers. *Phys. Rev. Lett.* **97**, 187401 (2006).
33. Dean, C. R. et al. Boron nitride substrates for high-quality graphene electronics. *Nat. Nanotechnol.* **5**, 722–726 (2010).
34. Nair, J. R., Gerbaldi, C., Destro, M., Bongiovanni, R. & Penazzi, N. Methacrylic-based solid polymer electrolyte membranes for lithium-based batteries by a rapid UV-curing process. *React. Funct. Polym.* **71**, 409–416 (2011).
35. Moser, J., Barreiro, A. & Bachtold, A. Current-induced cleaning of graphene. *Appl. Phys. Lett.* **91**, 163513 (2007).
36. Haider, M., Hartel, P., Müller, H., Uhlemann, S. & Zach, J. Information transfer in a TEM corrected for spherical and chromatic aberration. *Microsc. Microanal.* **16**, 393–408 (2010).
37. Malis, T., Cheng, S. C. & Egerton, R. F. EELS log-ratio technique for specimen-thickness measurement in the TEM. *J. Electron Microsc. Tech.* **8**, 193–200 (1988).
38. Kresse, G. & Furthmüller, J. Efficient iterative schemes for ab initio total-energy calculations using a plane-wave basis set. *Phys. Rev. B* **54**, 11169–11186 (1996).
39. Kresse, G. & Joubert, D. From ultrasoft pseudopotentials to the projector augmented-wave method. *Phys. Rev. B* **59**, 1758–1775 (1999).
40. Perdew, J. P., Burke, K. & Ernzerhof, M. Generalized gradient approximation made simple. *Phys. Rev. Lett.* **77**, 3865–3868 (1996).
41. Björkman, T. Van der Waals density functional for solids. *Phys. Rev. B* **86**, 165109 (2012).
42. Monkhorst, H. J. & Pack, J. D. Special points for Brillouin-zone integrations. *Phys. Rev. B* **13**, 5188–5192 (1976).
43. Momma, K. & Izumi, F. VESTA: a three-dimensional visualization system for electronic and structural analysis. *J. Appl. Cryst.* **41**, 653–658 (2008).
44. Virtual NanoLab v. 2016.4 www.quantumwise.com (QuantumWise, 2016).
45. Nelhiebel, M. et al. Theory of orientation-sensitive near-edge fine-structure core-level spectroscopy. *Phys. Rev. B* **59**, 12807 (1999).
46. Blaha, P., Schwarz, K., Madsen, G. K. H., Kvaniscka, D. & Luitz, J. *WIEN2k, an Augmented Plane Wave + Local Orbitals Program for Calculating Crystal Properties* (ed. Schwarz, K.) (Techn. Universität Wien, Austria, 2001).
47. Schwarz, K. DFT calculations of solids with LAPW and WIEN2k. *J. Solid State Chem.* **176**, 319–328 (2003).
48. Persson, K., Hinuma, Y., Meng, Y. S., Van der Ven, A. & Ceder, G. Thermodynamic and kinetic properties of the Li-graphite system from first-principles calculations. *Phys. Rev. B* **82**, 125416 (2010).
49. Thinius, S., Islam, M. M., Heitjans, P. & Bredow, T. Theoretical study of Li migration in lithium-graphite intercalation compounds with dispersion-corrected DFT methods. *J. Phys. Chem. C* **118**, 2273–2280 (2014).
50. Ganesh, P. et al. Binding and diffusion of lithium in graphite: quantum Monte Carlo benchmarks and validation of van der Waals density functional methods. *J. Chem. Theory Comput.* **10**, 5318–5323 (2014).
51. Leggesse, E. G., Chen, C.-L. & Jiang, J.-C. Lithium diffusion in graphene and graphite: Effect of edge morphology. *Carbon* **103**, 209–216 (2016).
52. Mandeltort, L. & Yates, J. T. Rapid atomic Li surface diffusion and intercalation on graphite: a surface science study. *J. Phys. Chem. C* **116**, 24962–24967 (2012).



Extended Data Fig. 1 | See next page for caption.

Extended Data Fig. 1 | Atomic resolution SALVE TEM images of lithium. **a**, Original TEM image (acquired between Fig. 2b, c). **b**, Same as **a**, but with graphene signals filtered out. **c**, Magnified view of area shown boxed in **b**. **d**, Slightly Gauss-filtered version of **c**. **e**, Same as **d**, but with red and blue circles indicating single Li atoms and symmetric positions without Li atoms, respectively. The latter show that the contrasts are not delocalization artefacts. **f**, Line profiles of the imaging contrast, centred on two neighbouring, individual Li atoms (left panel) and on the negative atomic contrast of a missing C atom in one graphene sheet, artificially inserted by the filtering procedure (right panel). The red arrows and red

dashed lines indicate the signal intensity of the respective atomic species. **g**, Fourier-filtered version (bilayer graphene lattice removed) of a TEM image acquired during lithiation at $t = 266$ s (bottom image), between Fig. 2b, c. The top row shows two zoom-ins centred on locations where the line profiles in **f** have been extracted. **h**, Temporal evolution of the C vacancy in one of the two graphene sheets from which the line profile in **g** has been extracted at $t = 266$ s. Each row corresponds to data from a single time: left, magnified sections of our TEM images as acquired; right, the same sections after the removal of the graphene lattice by Fourier filtering. Scale bars, 1 nm.

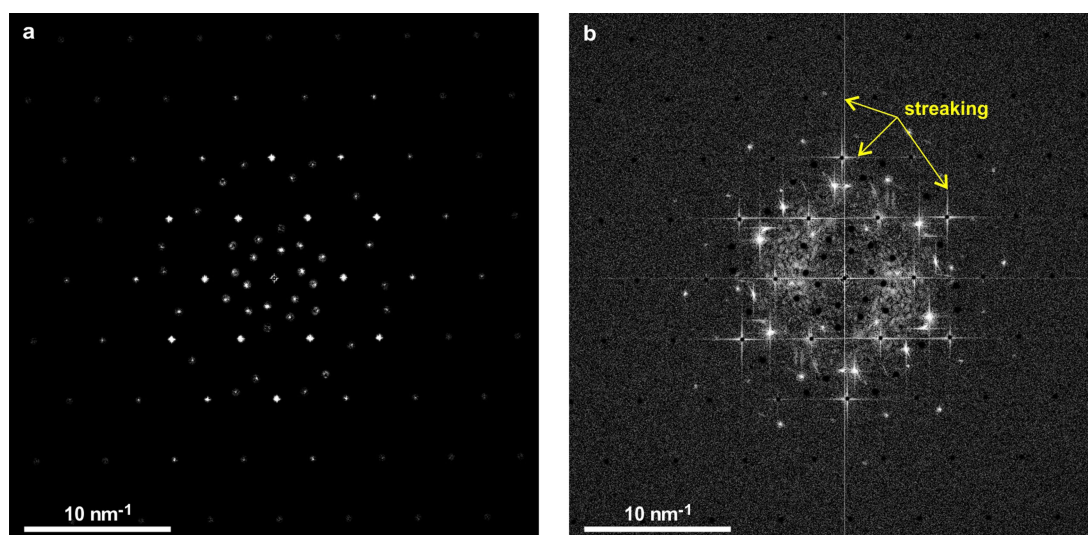


Extended Data Fig. 2 | See next page for caption.

Extended Data Fig. 2 | 80 kV SALVE TEM image simulations.

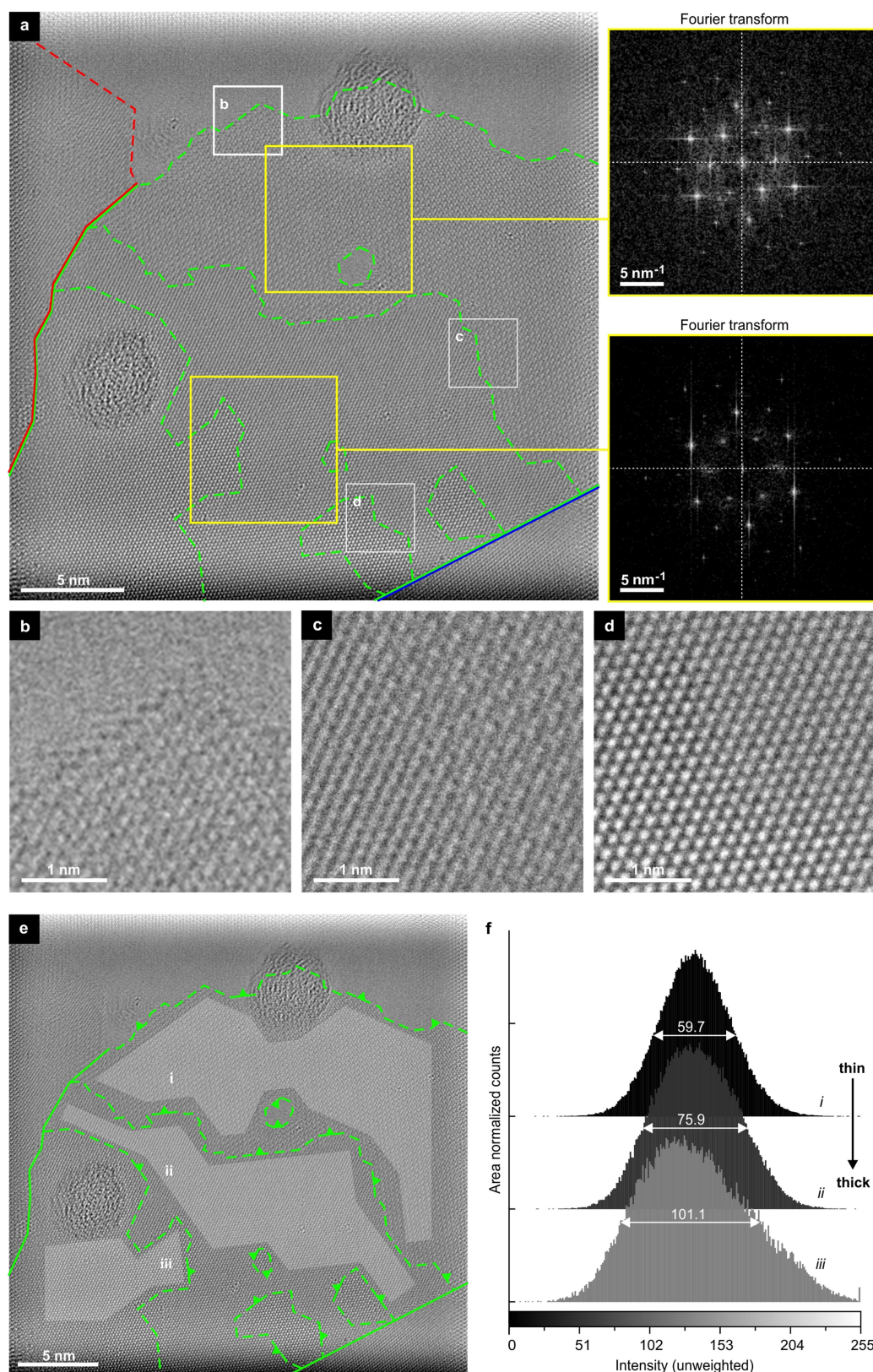
a, b, Atomistic model of a hexagonal close-packed Li wedge (red), with five additional single Li atom rows at its left edge as well as with single-atom vacancies, between two graphene sheets (cyan). Shown are a three-dimensional representation (**a**, top), a side view (**a**, bottom), and a top view of its thin front without C lattices (**b**). **c–e**, 80 kV dose-limited (applied dose $2 \times 10^6 \text{ e}^- \text{ nm}^{-2}$) TEM image simulations. **c**, Embedded in graphene. **d**, Fourier-filtered image with graphene removed. **e**, Unfiltered image simulated without graphene. In **d** and **e**, the yellow arrows mark single Li atoms and the white arrows point to a vacancy in the Li lattice.

f, g, Image simulation of wedges of two different close-packed Li systems (cubic and hexagonal shown at left and right, respectively). **f**, Atomistic model used for the simulations, showing side and top views. The thickness gradually increases by one layer from left (one layer) to right (six layers). **g**, Image simulations for two different values of defocus, seen along [111] for cubic close-packed Li and along [0001] for hexagonal close-packed Li. The von Hann-filtered Fourier transforms on the right (diffractograms) are calculated for 4 layers at +6 nm overfocus. For the simulation the corresponding experimentally measured electron dose was applied.



Extended Data Fig. 3 | Fourier filtering. Filtering mask for removing the graphene lattice and the moiré effects. **a**, Portion of the signal cut out by the applied mask. **b**, Remaining Fourier transform. The streaking

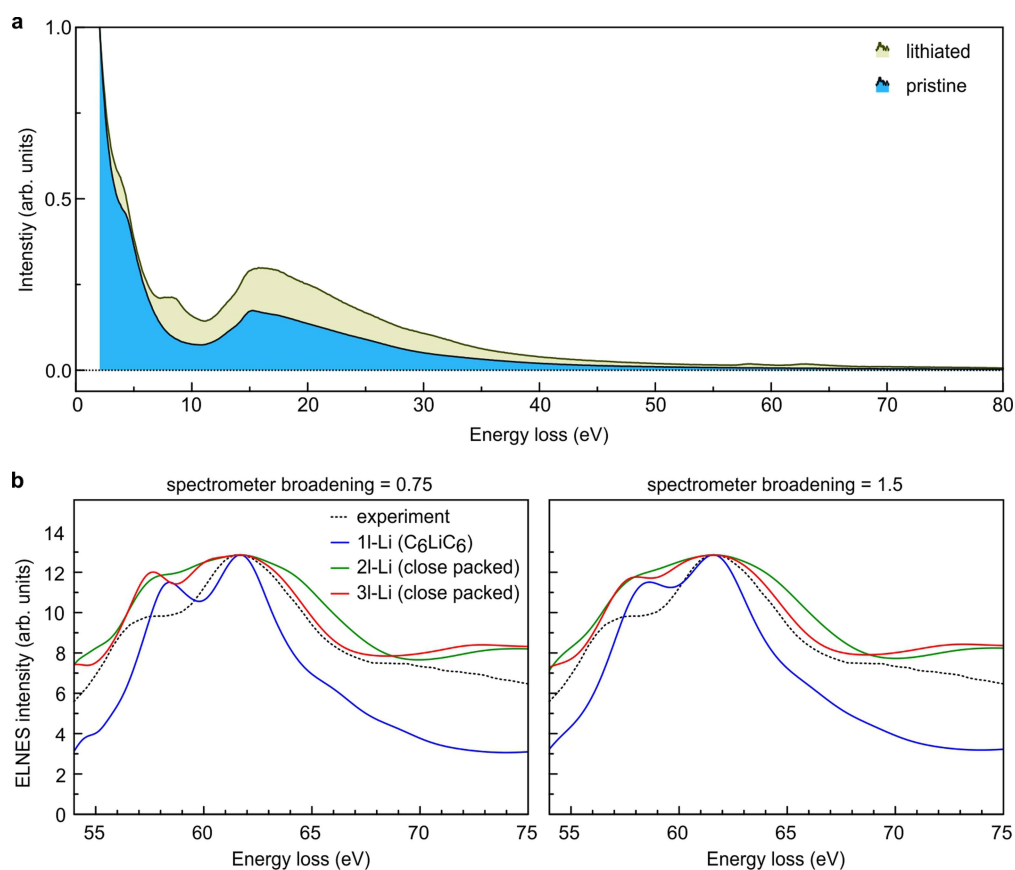
(indicated by yellow arrows) results from the edges of the real image and was not Fourier-filtered to avoid masking too-large portions of Fourier space.



Extended Data Fig. 4 | Thickness determination of crystalline Li.

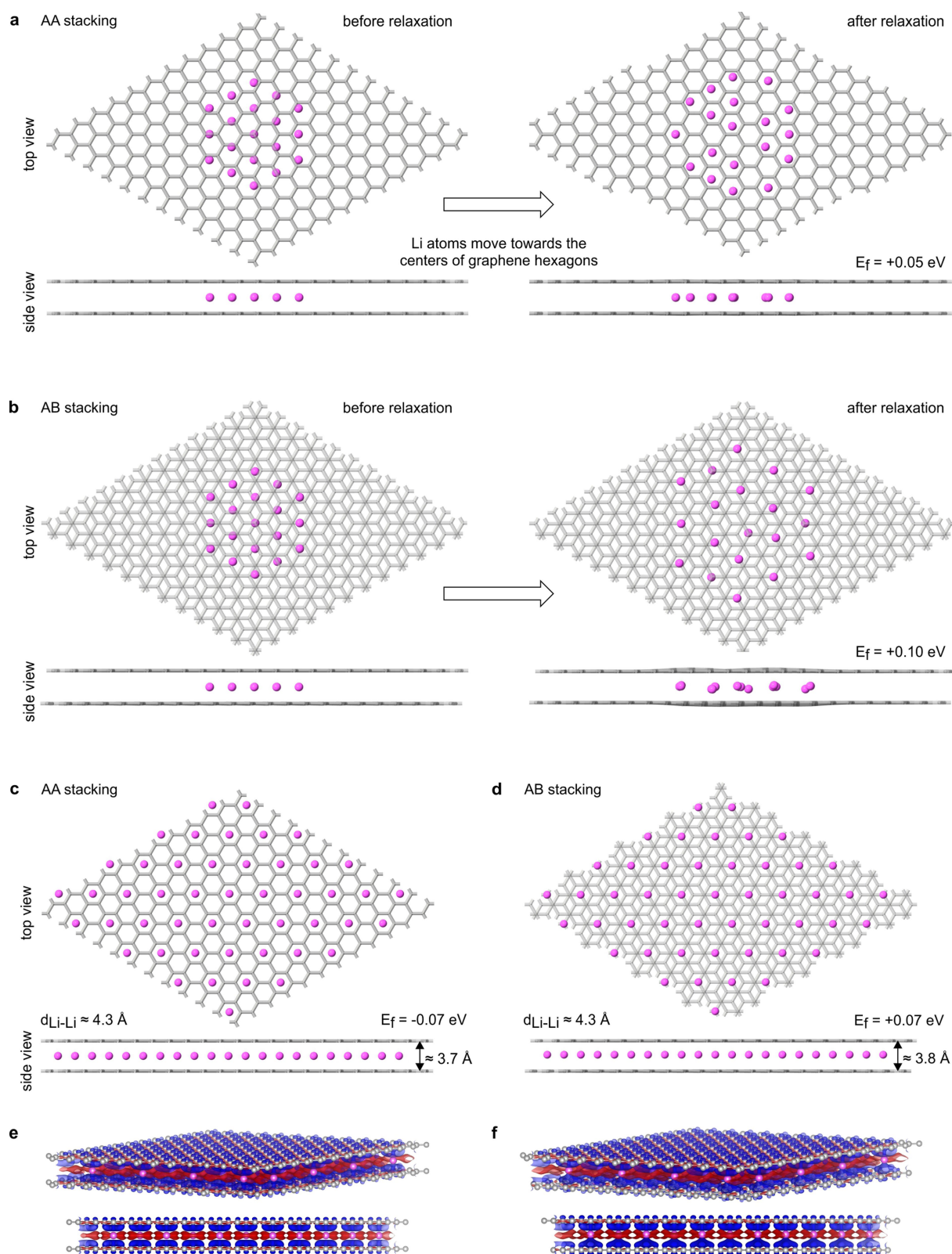
a, Main panel, Fourier-filtered TEM image. Dashed lines demarcate major edges enclosing regions of the Li phase with approximately constant thickness. Two-coloured lines demarcate grain boundaries. Fourier transforms from two selected regions of different thickness (yellow boxes) are shown on the right. Signals from the Li phase in the Fourier transforms for both regions lying within one grain are identical. **b–d**, Magnified views of selected areas of the TEM image (white boxes) in **a**. **e**, Relative

thickness determination from contrast quantification. **e**, Fourier-filtered TEM image (graphene lattice removed), identical to the main panel in **a**. Dashed lines demarcate major edges enclosing regions of the Li phase with approximately constant thickness. Arrowheads point outwards from thicker areas. **f**, Area-normalized intensity histograms acquired from the shaded regions in **e** that are labelled i, ii and iii. The full-widths at half-maximum (FWHMs) are indicated by white double-headed arrows.



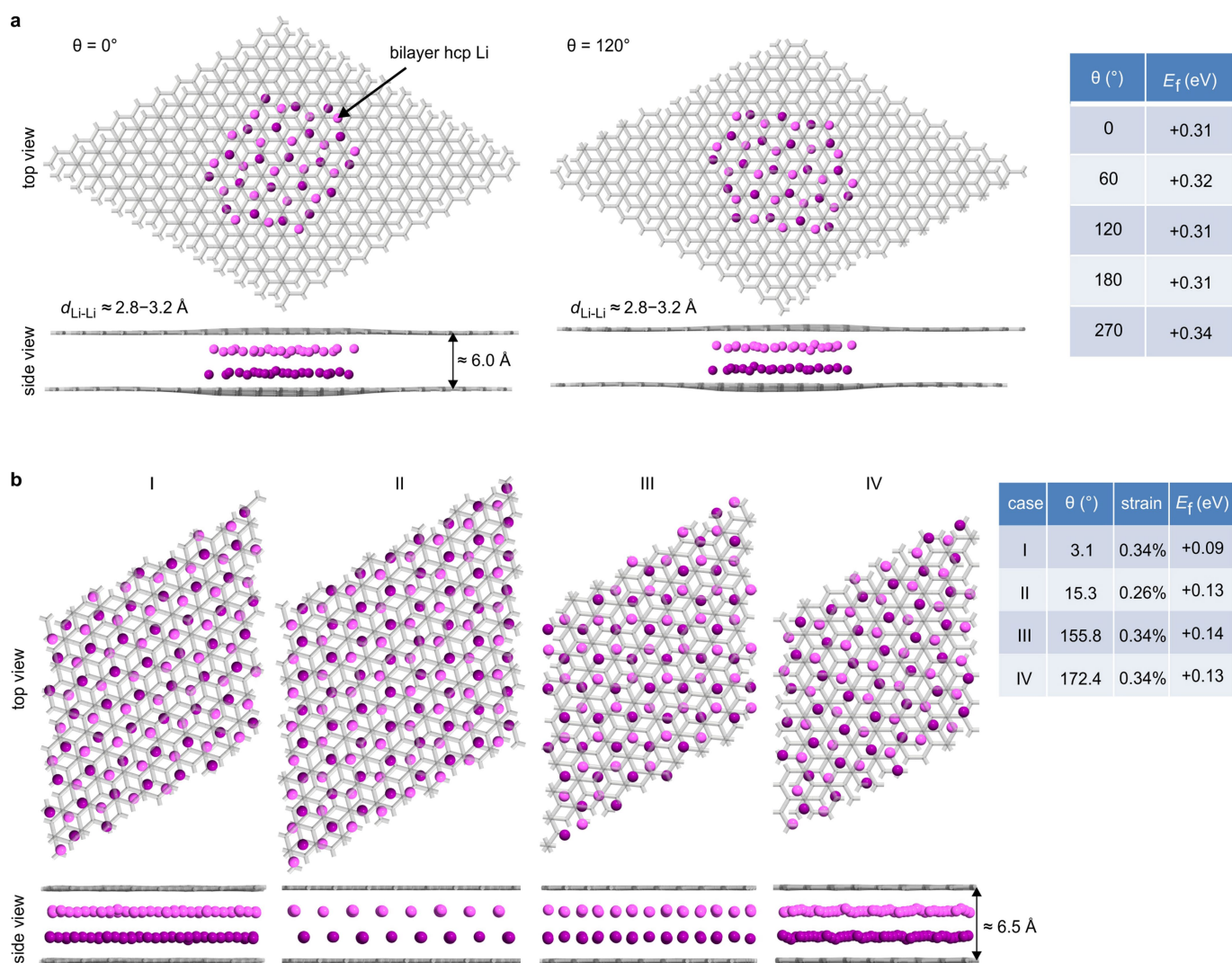
Extended Data Fig. 5 | Electron energy-loss spectroscopy. **a**, Low-loss EEL spectra of pristine (blue) and lithiated (yellow) bilayer graphene, with the close-packed Li phase present in the latter case. **b**, Calculated ELNES (electron energy loss near-edge structure; Methods) of the Li-K edge for bilayer graphene containing 1, 2 and 3 Li layers compared

to the experimental ELNES. The spectrometer broadening is taken into account by convoluting the result with a Gaussian function. Two different broadenings have been considered (left and right panels). The spectrometer broadening is given as the FWHM of the respective Gaussian function.



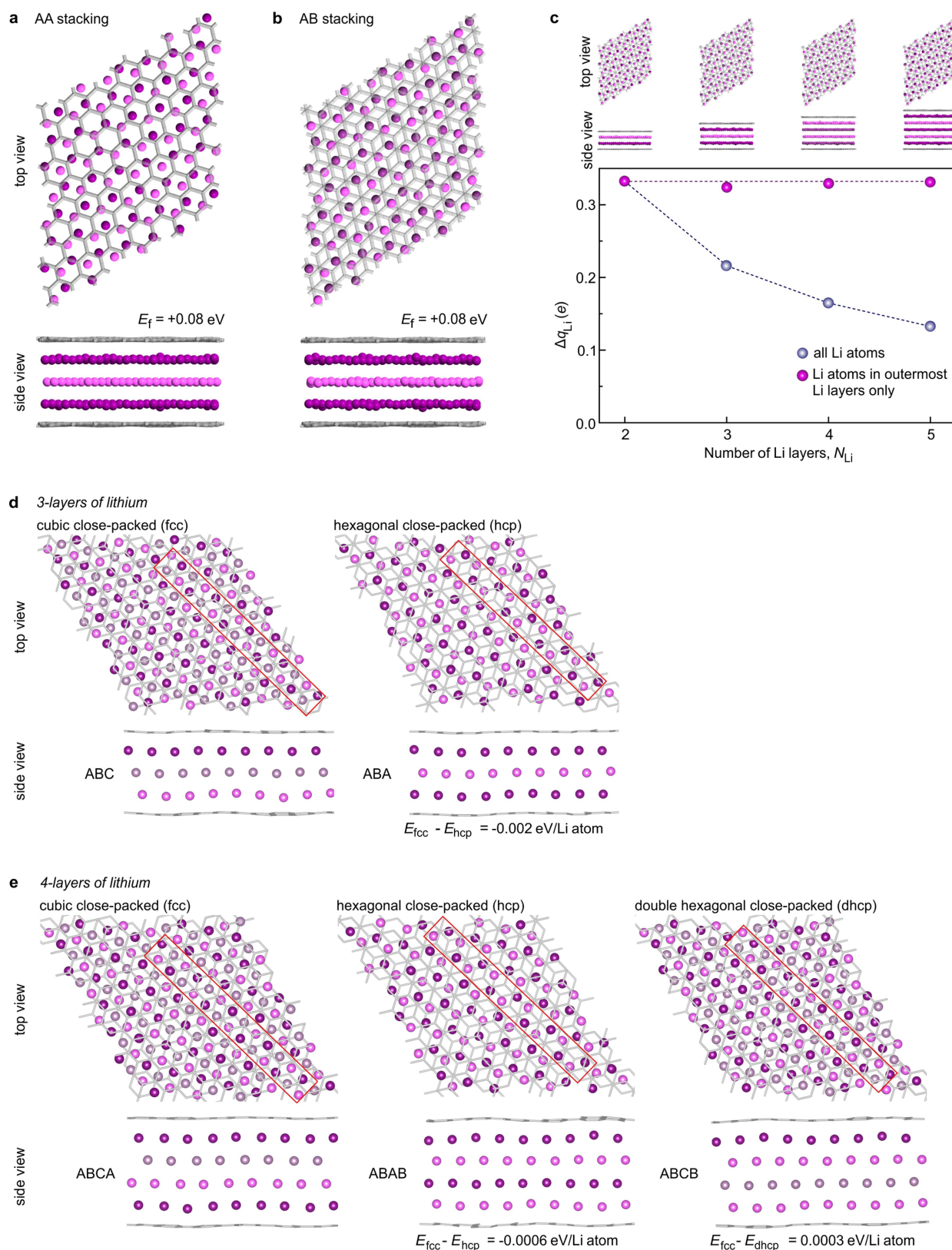
Extended Data Fig. 6 | Atomic configurations and energetics of a single layer of Li atoms between two graphene sheets. **a, b**, Structural evolution of a finite single-layer cluster of Li atoms between two graphene sheets with different stacking: AA-stacking (**a**) and AB-stacking (**b**). Left and right structures are before and after relaxation (that is, energy minimization); top and bottom are top and side views, respectively. The relaxation gives rise to the formation of a system with a geometry close to the C_6LiC_6 configuration. Note that the configurations correspond to a local, not global, energy minimum. **c, d**, The periodic C_6LiC_6

configuration with Li atoms arranged in a commensurate $(\sqrt{3} \times \sqrt{3})\text{R}30^\circ$ superstructure between graphene sheets for AA stacking (**c**) and AB stacking (**d**). $d_{\text{Li-Li}}$ refers to the separation of Li atoms. Double-headed arrows indicate the spacing between graphene sheets. **e, f**, Electron density difference between the combined system and its isolated parts. Red colour corresponds to a decrease in the electron density, blue to an increase. Charge transfer between Li and graphene (with an average value of 0.85 electrons per Li atom) is clearly observable.



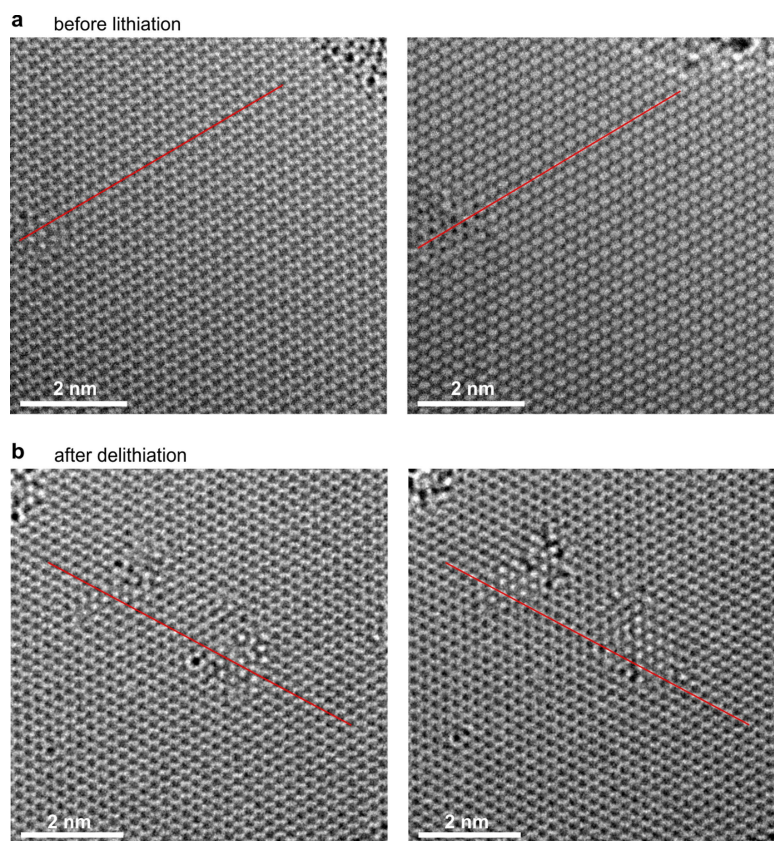
Extended Data Fig. 7 | Atomic configurations and energetics of Li bilayers between two graphene sheets. a, The geometric arrangement of the atoms of a finite bilayer cluster of Li atoms encapsulated between two graphene sheets after energy minimization for two different rotation angles θ between the Li and C lattices. The original configuration of the cluster was the perfect h.c.p. lattice. The structure is largely preserved during the relaxation. The distance between the Li atoms is denoted as $d_{\text{Li-Li}}$. A very weak dependence on the angle between graphene and h.c.p.

lattice is found, as shown in the table at right. **b,** Atomic configurations and energetics of the infinite commensurate Li bilayer h.c.p./graphene structure and the dependence of the energy on the orientation angle θ between surfaces. Very weak dependence on the angle between graphene and the h.c.p. Li lattice is found. A small amount of strain introduced into the system to make the graphene and Li lattices commensurate affects the results by no more than 0.01 eV, as evident from the tables presenting E_f for different θ .



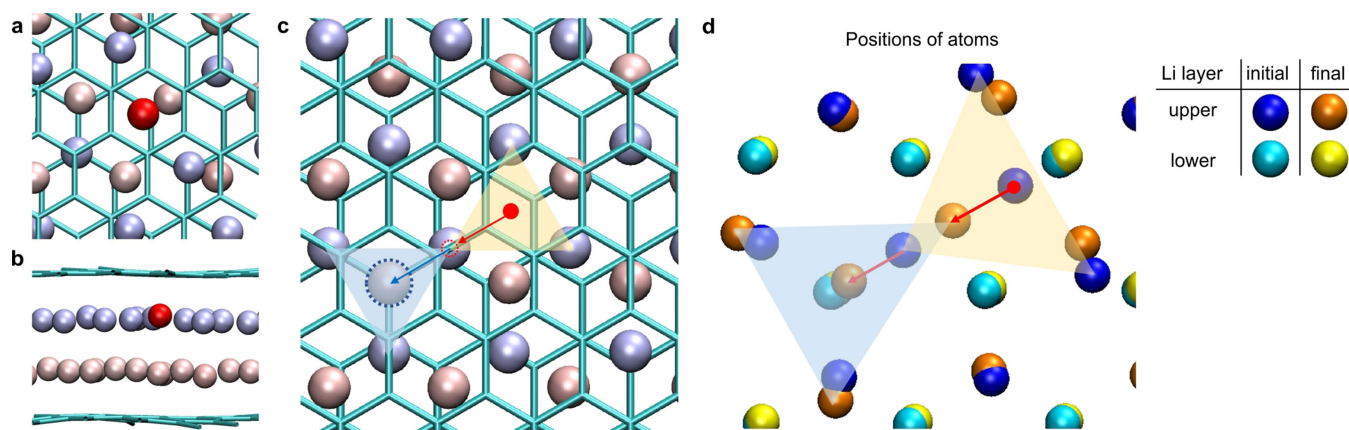
Extended Data Fig. 8 | Atomic configurations and energetics of Li multilayers between two graphene sheets. **a, b**, Atomic configurations and energetics of the infinite commensurate Li trilayer with h.c.p. structure between two graphene sheets for AA stacking (**a**) and AB stacking (**b**). **c**, Main panel, charge transfer from Li to graphene as a function of the number of close-packed Li layers N_{Li} between two graphene sheets. The corresponding atomic configurations are shown above the plot. The blue values are obtained as $\Delta q_{Li} = q_0 - q_{Li}$, where q_{Li} is the charge of Li after intercalation and q_0 is the charge of the isolated

Li atom. Since the charge transfer is relevant for outermost Li layers only, we also plot the full charge transfer renormalized by the number of Li atoms in these outermost Li layers without considering the other Li layers (purple). **d, e**, Energy difference between different possible close-packed configurations (stacking orders), calculated for three layers of Li between two graphene sheets (**d**) and four layers of Li between two graphene sheets (**e**). To illustrate the stacking order, below each top view we include a side view of atoms within the red rectangle. The energy differences with respect to each f.c.c. case are stated below the side views.



Extended Data Fig. 9 | Registry of graphene layers. a, b, Successive SALVE TEM images at different defocus values before lithiation (**a**) and after delithiation (**b**). The red lines are guides for the eye. We do not observe a change in registry of the two graphene sheets when comparing

TEM images of the graphene lattice before lithiation and after delithiation. The registry can be checked at sites where one of the two graphene sheets features a moderately big hole. The stacking is AB without any sign of change throughout the experiment.



Extended Data Fig. 10 | Lateral diffusion of a Li atom inside the close-packed Li system confined between two graphene sheets. **a, **b****, Schematic atomistic configuration (top and side view). The red sphere represents the extra interstitial Li atom. **c**, Schematic of the diffusion process. **d**, The actual initial/final positions of atoms. The yellow and blue transparent

triangles in **c** and **d** mark the initial and final configurations of the interstitial atom with regard to the nearest Li atoms in the undistorted (**c**) and the optimized (**d**) structures. The red and blue arrows connect the initial and final positions of the diffusing atoms.